nature physics

Supplementary information

https://doi.org/10.1038/s41567-025-03132-z

Driving Floquet physics with excitonic fields

In the format provided by the authors and unedited

Contents

Background correction for ARPES data

To clearly visualize the Optical Floquet replica, the ARPES data was corrected to remove the background signal from the extended tail of the valence band. The background signal was removed using an asymmetric least square smoothing algorithm. Supplementary figure 1 shows the ARPES data before and after the correction for the optical Floquet replicas, where the signal from the replica remains untouched but can be seen more clearly.

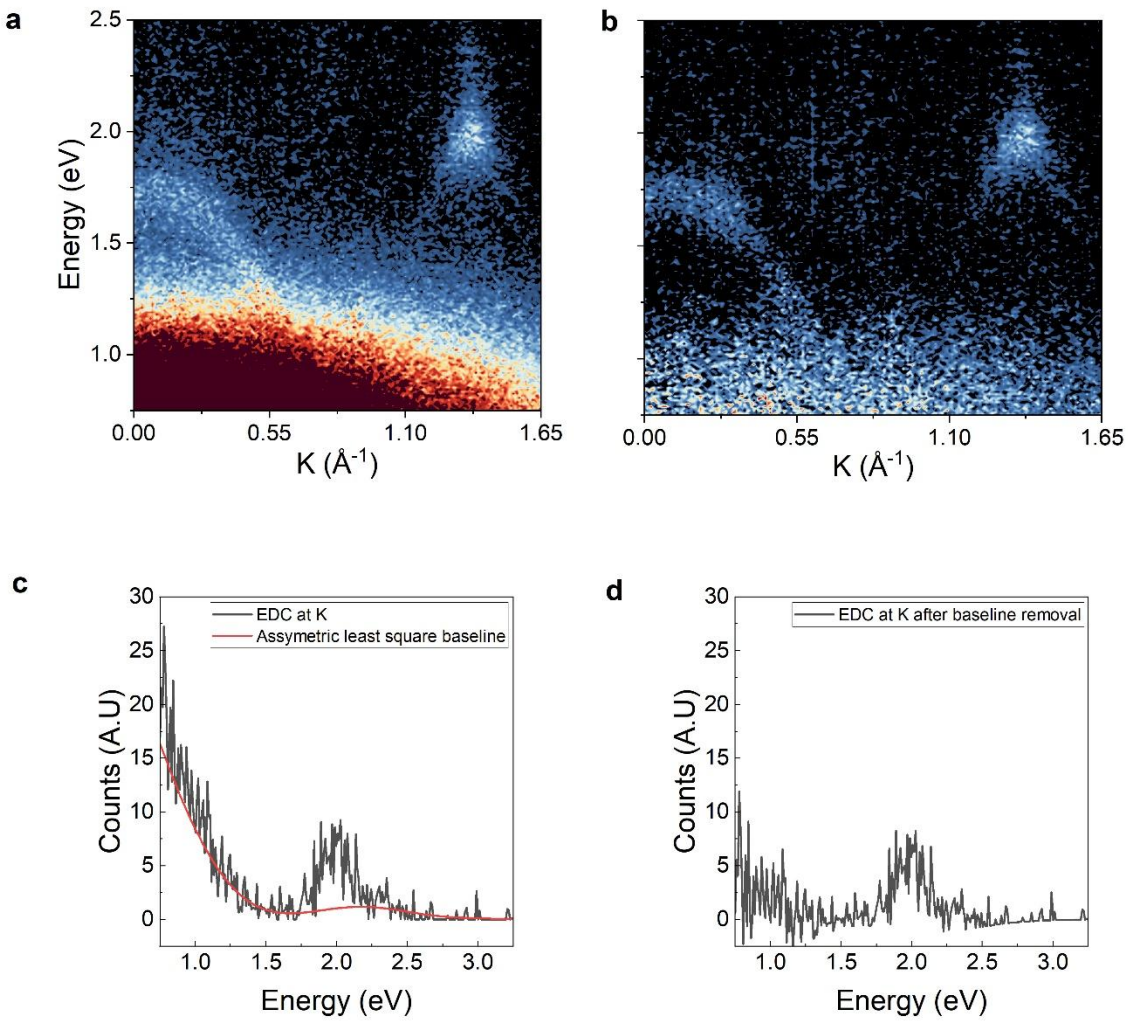

Supplementary figure 1 Background subtraction for Optically driven Floquet: *a) Bandstructure showing the optically driven Floquet replica at 1.98 eV. The color profile is saturated to show the replica clearly. b) The replica after the background subtraction. c) EDC at the K point (yellow dotted line) along with the background obtained from the asymmetric least square smoothing algorithm. d) EDC at the same point (yellow dotted line) after the background subtraction. The Floquet replica is more clearly visible after the background subtraction.*

Difference between Volkov and Floquet state

Supplementary figure 2 shows the optical Floquet state and the Volkov state for 1.98 eV pump excitation. The Volkov and the Floquet state have different origins but have identical photoemission signals[7,8]. However, the two processes can be distinguished by choosing the correct pump polarization. For the *p*-polarized pump, the photoemission signal has

contributions from both the Volkov and the Floquet states. For the case of *s*-polarization, only Floquet states contribute to the signal. This is further evidenced by the difference in

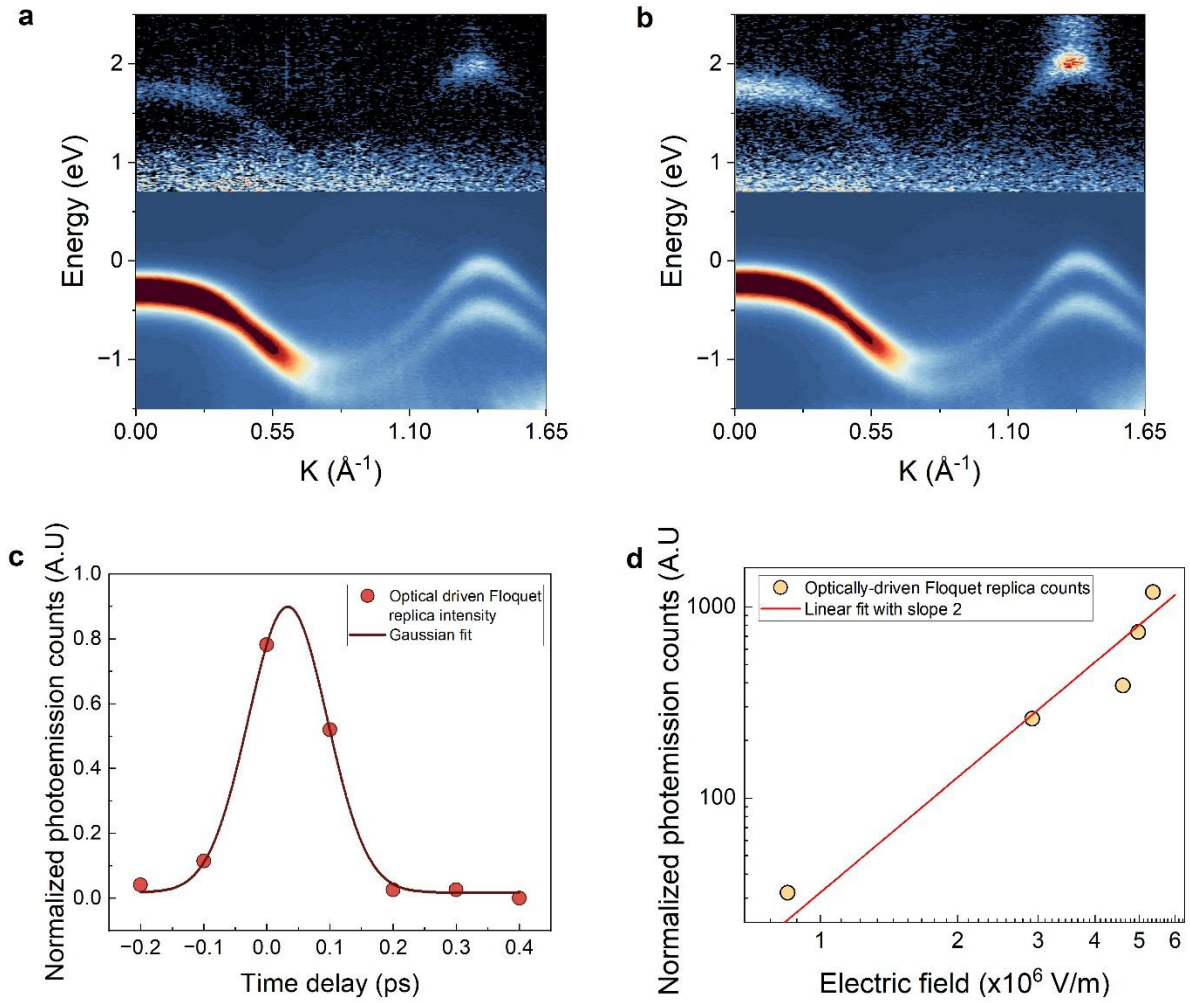

Supplementary figure 2 Comparison between Optically driven Floquet and pump-induced Volkov states: *a) Optically driven Floquet replica for the s-polarized pump pulse, b) Pump-induced Volkov state together with optically driven Floquet replica for the p-polarized pump pulse. c) The optically driven Floquet replica lasts for ~130 fs corresponding to the cross-correlation between the pump and the probe beams. The photoemission counts from the Optically driven Floquet replica was obtained by integrating a small momentum range (± 0.2 Å^{-1}) and energy range ($\pm 0.2\ eV$) around the gamma point replica. The duration of the optically driven Floquet replica was obtained from the FWHM of the single gaussian fit to the photoemission counts (red curve). We expect the Volkov states to last for similar duration as optically driven Floquet replica. d) log-log plot of the normalized photoemission counts from the optically driven Floquet replica versus the applied optical electric field strength. The photoemission counts show a quadratic behavior in applied electric field strength as confirmed by the slope 2 of the linear fit (red line) in the log-log plot.*

the relative strengths of the replica signature we observe for the two different polarization cases. For the *p*-polarized excitation, the replica strength is 4% of the valence band, whereas the replica for the *s*-polarized case is only 2% of the valence band signal. The optically driven Floquet replica was observed for ~130 fs due to the finite pulse width of the pump and the probe pulse in our experiments. Moreover, the photoemission counts scale quadratically with the electric field strength as seen in the log-log plot in Supplementary Figure 2.

Confirmation of valence band dispersion change

To ensure that the observed Mexican-hat-like dispersion is indeed due to exciton driven Floquet effect and not an artefact of the exciton-bound holes in the valence band, we compared the measured energy distribution curve at each k vector before photoexcitation in the ground state, and in the presence of a high-density of excitons. The curves are obtained and calibrated so that one can directly compare the photoemission intensity before and after photoexcitation. For calibration, we first consider the EDCs at *k* vectors that are unaffected by the photoexcitation of the holes, *i.e.*, *k* vectors away from the center of the K valley (e.g., k_x = -0.1 Å^{-1} in Fig 2c). We scale the photoexcited EDC at k_x =-0.1 Å^{-1} such that the area under the curve for the photoexcited and unphotoexcited curve are equal. We then scale the rest of the photoexcited EDCs at all other k vectors with the same scaling factor to allow for a direct comparison with the unphotoexcited EDCs near the center of the K valley. Such calibration allows us to correct for variations in the experimental conditions between measurements. A few such comparisons are shown in Fig. 2C. In the case of the ground-state, we see a symmetric, Gaussian-shaped energy distribution with a FWHM of ~60 meV at the center of the K valley (corresponding to the relatively low inhomogeneous broadening of our sample), and a slightly more broadened distribution (FWHM ~60 – 100 meV) as we move away from the center of the K valley (due to the shorter lifetime of holes away from the valley center). For the measurements in the presence of a high-density of excitons, we continue to see a *symmetric, Gaussian-shaped* energy distribution, now with a k-dependent peak-energy shift, broadening and decreased signal (i.e., area under the curve). The k-dependent decrease in the signal exactly corresponds to the density of exciton-bound holes at the given k vector, as reported previously[1]. In contrast, the k-dependent *shift in peak energy* corresponds to the change in the dispersion of the valence band discussed in this manuscript (supplementary figure 3). As can be seen (Fig. 2c), the shifts in the peak energy cannot be an artefact

due to the presence of holes, as the shifts are too large relative to the ground-state linewidth.

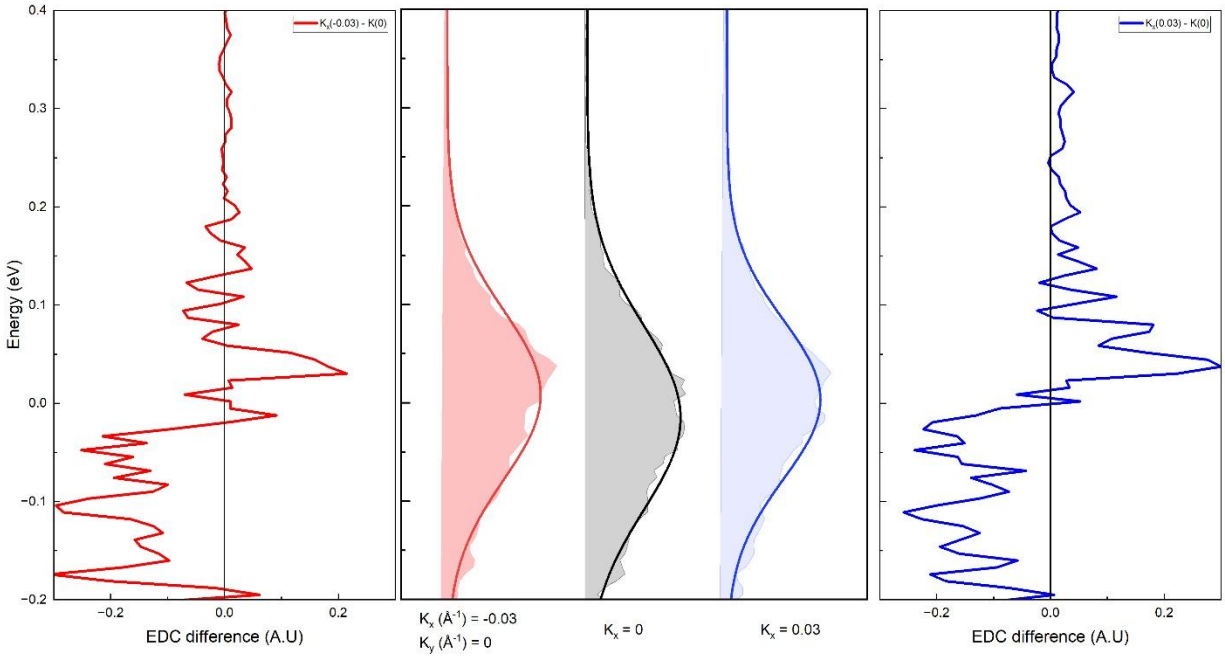

Supplementary figure 3 Identifying small peak energy differences in the electronic distributions in the valence band near K point: *The difference between the energy distribution curve at K point and at a) Kx = -0.03 A^{-1} and b) 0.03 A^{-1}. The plot clearly shows the characteristic positive-negative step like function corresponding to a small shift to lower energy at the center of the VB relative to that at finite k-vectors away from the center. The plots in the center are the EDCs at K_x = -0.03, 0, and 0.03 A^{-1} . The solid lines are the gaussian fitting to the EDCs.*

Measurements at 200 fs and earlier fall within excitonic coherence time in our system

To confirm our measurement at 200 fs falls within the excitonic coherence, we provide four independent arguments and evidence, including our latest time-resolved measurement of the exciton Floquet effect:

a) First, we note that a coherence time of few hundred femtoseconds in monolayer WS_2, at temperatures similar to our experimental conditions, has been reported in literature[2]. In particular, at 100 K – the temperature of our TR-ARPES measurements – the measured coherence time is $\tau_{coh}=2\hbar/\gamma_{hom}$ ~ 350 fs, corresponding to a *homogeneous* excitonic linewidth γ_{hom} of about 3.8 meV. Thus, our measurements at 200 fs and earlier, fall well within this expected coherence time.

b) Next, we measured the excitonic absorption linewidth at 100 K in our sample, obtaining a value of $\gamma = 8\,meV$. This value is significantly smaller than typical samples (see[3]), and is comparable to that obtained in high quality samples at ~100K. This measured absorption linewidth is the sum of the homogeneous and the inhomogeneous contributions. In high-quality samples, these two contributions have been reported to be comparable in value [4], thus giving us $\gamma_{hom} \sim 4\,meV$, consistent with literature noted in (a) above, and giving us a coherence time of few hundred femtoseconds.

c) Another estimation of the coherence time comes from the relationship between the homogeneous linewidth and the population relaxation rate Γ, which is given by: $\gamma_{hom} = \Gamma/2 + \gamma^*$, where γ^* accounts for processes such as exciton-phonon interactions[5]. In Fig. 3a, we plot the measured exciton population n_x as a function of time-delay, and obtain a population decay time of τ=800 fs, from which, we extract $\Gamma = 2\hbar/\tau$=1.6 meV. From recent calculations as in ref[6], γ^* is estimated to be ~3 - 6 meV. This provides another independent estimation of $\gamma_{hom} \sim 3.8 - 6.4\,meV$, corresponding to a coherence time of ~210 – 350 fs. Again, this is consistent with literature, our exciton absorption measurement, and supports our claim that measurements at 200 fs and earlier fall within the coherence time of our system.

d) Finally, in Fig.3a, we plot ΔE_X – the decrease in energy at the center of the valence band in the presence of excitons (i.e. a quantitative measure of the Mexican hat like dispersion) – as a function of time-delay. This experimentally challenging measurement gives us the timescale of the exciton-Floquet effect to be ~470 fs. Within experimental error, this is consistent with the above arguments that coherence time is expected to be few hundred femtoseconds.

In conclusion, these four independent arguments and experimental evidence strongly support our claim that our reported measurements of exciton-driven Floquet at 200 fs and earlier fall within the coherence time of the system.

K and Q valley photoemission intensity

For the exciton-driven Floquet experiments, we perform all our experiments at short enough time delay (0.2 ps) such that exciton-phonon interactions are relatively minimal as seen from the very weak photoemission intensity in the Q valley as compared to the K valley (Supplementary Figure 4).

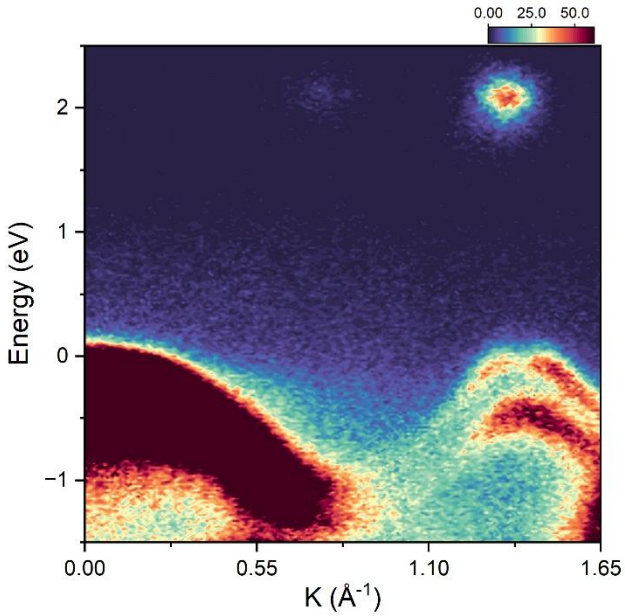

Supplementary figure 4 Photoemission intensity at K and Q valley: *The $\Gamma - K - M$ cut for the highest exciton density ($n_X = 3 \times 10^{12}\ cm^{-2}$). Photoemission signal at the K valley is more than an order of magnitude stronger compared to the intensity at the Q valley.*

Relation between TD-aGW self-energy, density, and exciton binding energy

In this section, we show that the effective electron-hole interaction is proportional to the square root of exciton density in the Method. We demonstrate this proportionality in a simple one-dimensional model, where the Hamiltonian is described by[9,10]

$$H = \sum_{\boldsymbol{k}} \left(\epsilon_{v\boldsymbol{k}} a^{\dagger}_{v\boldsymbol{k}} a_{v\boldsymbol{k}} + \epsilon_{c\boldsymbol{k}} a^{\dagger}_{c\boldsymbol{k}} a_{c\boldsymbol{k}}\right) - U \sum_{\boldsymbol{k}} n_{\boldsymbol{k}} + \frac{U}{N} \sum_{\boldsymbol{k}_1, \boldsymbol{k}_2, \boldsymbol{q}} a^{\dagger}_{v\boldsymbol{k}_1+\boldsymbol{q}} a^{\dagger}_{c\boldsymbol{k}_2-\boldsymbol{q}} a_{c\boldsymbol{k}_2} a_{v\boldsymbol{k}_1},$$

where $\epsilon_{v\boldsymbol{k}}(\epsilon_{c\boldsymbol{k}})$ is the band energy of the valence (conduction) band with wavevector $\boldsymbol{k}$, U is the on-site interaction between two bands, and N is the number of sites. The energy dispersion is given by $\epsilon_{v\boldsymbol{k}} = -2(1 - cos\,\boldsymbol{k}) - E_g/2$, and $\epsilon_{c\boldsymbol{k}} = -\epsilon_{v\boldsymbol{k}}$ with $E_g = 1$ in our choice of system of units.

We demonstrate that the effective electron-hole interaction $\delta\Sigma_{vc\boldsymbol{k}}$ is proportional to the square root of carrier density in Supplementary figure 5 by gathering data at different pump setup.

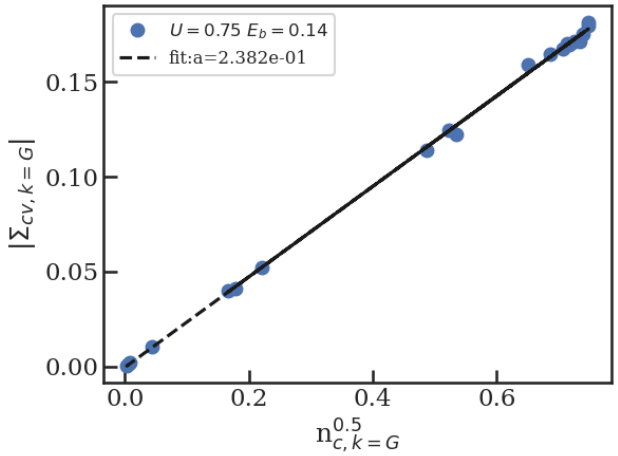

Supplementary figure 5*. Effective interaction as a function of the square root of density.*

Band renormalization from T-matrix calculations

In the incoherent regime, band renormalization and spectral function features can be computed from a T-matrix approximation[11–14], where the electron-hole ladder diagram is summed as the self-energy. Calculations employing the T-matrix formalism naturally capture finite temperature effects and the photoinduced change in the electronic screening. However, owing to the computational challenge, performing a first-principles T-matrix calculation remains elusive. To gain qualitative insights, we construct a two-band model including one valence and one conduction bands for a T-matrix calculation[14]. The band renormalization at valence band maximum is shown below in Supplementary figure 6. We observe similar linear scaling trends between the TD-aGW and T-matrix calculations for the strength of the hybridization of the state at the VBM. We also note that, consistent with previous T-matrix calculations[13], we do not see a negative dispersion of the replica band for the calculations performed at 100K and 300K. This corroborates the fact that, at times 200 fs after the optical pump, the system is still coherent and hence well described by TD-aGW. A fully incoherent approach, such as that of the T-matrix formalism, fails to adequately capture the replica bands.

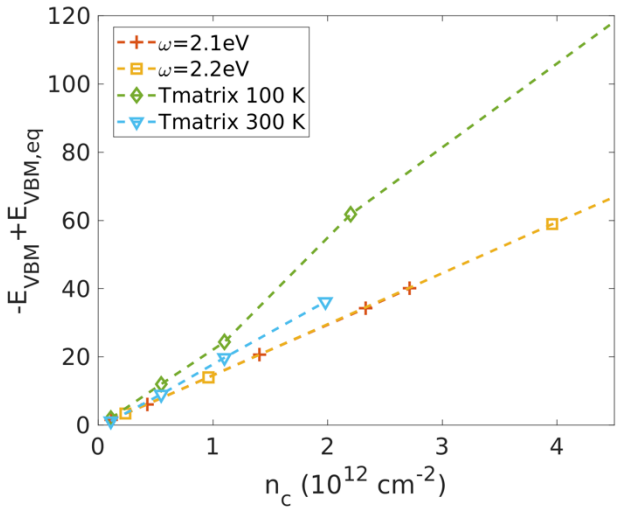

Supplementary figure 6 *Comparison of the band renormalization at VBM, evaluate with our model-Hamiltonian calculation using a T-matrix approximation to the self-energy and with the first-principles TD-aGW approach, as a function of the density of excited conduction-band electrons (a proxy for the exciton density).*

Details of T-matrix calculations

The full dynamics of excited electrons and holes with many-body effects can in principle be solved from first principles with the nonequilibrium Green's function formalism. However, such full first-principles method has remained computationally demanding. Instead, we consider a quasi-equilibrium case where the time-dependence of the system may be specified by some time-dependent quantities (such as the electron and hole density) which are slowly varying in time. At a given time, the system's behavior may be described in terms of these instantaneous quantities within a quasi-equilibrium (and therefore incoherent) framework. Under such approximation, our system is modeled by an electron temperature and two chemical potentials, one for electrons and one for holes. The detailed justification of the usage of the quasi-equilibrium theory for understanding time-resolved dynamics has been discussed in Ref.[15]. The key point is that due to the large separation in time scale of different scatterings, the system evolves slowly after the first hundred fs. Therefore, within the probe window the system can be considered as a quasi-equilibrium state with an averaged number of excitation density. The quasi-equilibrium theory has been successfully applied in different contexts[16–21].

T-matrix self-energy and ladder diagram

The interacting single-particle Green's function and the spectral function can be obtained following the equilibrium Green's function formalism with a self-energy approximation to many-body effects. To incorporate the excitonic correlation on the behavior of excited electrons and holes, we evaluate the electron-hole ladder diagram for the self-energy Σ[12,13,15,22], which reads, $\Sigma(t,t') = -iT(t,t')G(t,t')$, where $G(t,t')$ is

the single-particle Green's function and $T(t,t')$ is the T matrix. The first three terms of the infinite ladder series are shown below:

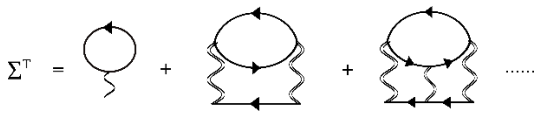

where the double-wavy line represents the screened Coulomb interaction, and the solid lines are electron or hole Green's function. The T matrix describes a series of electron-hole scattering via screened Coulomb potential. The possibility of forming bound states (excitons) has been considered in the ladder-diagram. Therefore, from the ladder-diagram self-energy, we can compute the band renormalization due to the excitonic correlations. This is different from the well-known GW self-energy which describes the dynamical screening effects but cannot capture excitonic interaction effects.

For calculating the T-matrix self-energy, we take the static approximation of the screened Coulomb interaction. Such approximation has been successfully used to describe excitonic effects in solving the BSE for optical properties of semiconductors from first-principles[23]. The detailed formalism of the T matrix theory has been given in earlier works. We adopt the formula for T-matrix self-energy from Ref.[13] and rewrite it into an appropriate form for our case, which reads,

$$\Sigma^{\mathrm{T}}_{\mu\boldsymbol{k}}(\omega)=\sum_{\lambda l}\frac{\left(\omega^{\boldsymbol{q}}_{\mu l\boldsymbol{k}-\boldsymbol{q}}-\Omega^{\lambda\boldsymbol{q}}\right)^2}{\left|f^{\boldsymbol{q}}_{\mu l\boldsymbol{k}-\boldsymbol{q}}\right|^2}\frac{1+\mathrm{n}_{\mu,l}(\Omega^{\lambda\boldsymbol{q}})-f_{l\boldsymbol{k}}\left(\epsilon_{l\boldsymbol{k}-\boldsymbol{q}}\right)}{\omega-\left(\Omega^{\lambda\boldsymbol{q}}+\epsilon_{l\boldsymbol{k}-\boldsymbol{q}}\right)+\mathrm{i}\eta}\left|\mathrm{A}^{\lambda\boldsymbol{q}}_{\mu l\boldsymbol{k}-\boldsymbol{q}}\right|^2,$$

where $f^{\boldsymbol{q}}_{\mu l\boldsymbol{k}-\boldsymbol{q}}=f_{\mu\boldsymbol{k}-\boldsymbol{q}}-f_{l\boldsymbol{k}}$ and $\omega^{\boldsymbol{q}}_{\mu l\boldsymbol{k}-\boldsymbol{q}}=\epsilon_{\mu\boldsymbol{k}-\boldsymbol{q}}-\epsilon_{l\boldsymbol{k}}$ are electron occupation and energy differences with band index μ, l and momentum $\boldsymbol{k}-\boldsymbol{q}$, $\boldsymbol{k}$, respectively, $\mathrm{A}^{\lambda\boldsymbol{q}}_{\mathrm{nm}\boldsymbol{k}}$ and $\Omega^{\lambda\boldsymbol{q}}$ are the exciton envelop function and energy of the state λ, respectively, $n_{a,b}(\omega)=\frac{1}{e^{\beta(\omega-\mu_a+\mu_b)}-1}$ is the Bose factor and μ_a is the chemical potential of the type a carriers.

We consider a screened Coulomb interaction when solving BSE. We further approximate the occupation differences to be their equilibrium values following Ref.[13], which ignores the Pauli-Blocking effects.

Calculation details

To model the electronic structure of a monolayer WS_2 near the K and K' valley, we use a two-band model with dispersions $\epsilon_{vk}=-\frac{k^2}{2m}$ and $\epsilon_{ck}=E_g+\frac{k^2}{2m}$, where $E_g=2.6$ eV and $m=0.314$ a.u are fitted from first-principle GW calculations. We consider excitations induced band renormalization from both T-matrix self-energy and GW self-energy following Ref.[11] where the latter is approximated with a sum of static screened exchange and Coulomb hole self-energy. We have

$$\Sigma_{n\boldsymbol{k}}^{SX} = -\sum_{\boldsymbol{q}} W(q) \int \frac{d\omega}{2\pi} f_{n\boldsymbol{k}-\boldsymbol{q}}(\omega) A_{n\boldsymbol{k}-\boldsymbol{q}}(\omega)$$

where $f_{n\boldsymbol{k}-\boldsymbol{q}}(\omega)$ is the Fermi-Dirac distribution of band n and momentum $\boldsymbol{k}-\boldsymbol{q}$ and $A_{n\boldsymbol{k}-\boldsymbol{q}}(\omega)$ is the corresponding spectral function. The Coulomb hole self-energy reads,

$$\Sigma_{n\mathrm{k}}^{COH} = \frac{1}{2}\sum_{k'} (W(k') - U(k'))$$

which is a constant overall shift in our model. The screened Coulomb interaction is modeled with the following form,

$$\mathrm{U}(q) = \frac{1}{a + bq + cq^2}$$

By fitting from *ab initio* calculations for monolayer WS_2, we obtained $a = 43.203$, $b = -3325.563$, and $c = 415401.123$ (in atomic units). Screening effects from excited carriers is included through $\mathrm{W}(q) = \epsilon^{-1}(q)\mathrm{U}(q)$, where the susceptibility and the dielectric function is modeled with that of the two-dimensional electron gas. We have the momentum and temperature dependent susceptibility[24],

$$\chi(q,T) = -\frac{4N_v m}{2\pi} \int_0^{\bar{q}/2} \mathrm{dx} \frac{\mathrm{F(x,T)}}{\bar{q}(\bar{q}^2 - 4\mathrm{x}^2)^{0.5}}$$

where the parameters $\bar{q} = q/k_F$, N_v is the number of valleys, and $F(x,T) = \frac{x}{e^{\beta\left(x^2 E_f - \mu\right)}+1}$.

The ladder diagram calculation is computationally expensive, so we consider k-points within an 0.15 Bohr^{-1} patch in a 64×64 grid around K or K' valleys. Electron-hole propagators are solved for all possible combinations of momentum within the patch. Excited carriers induced screening effects are considered while Pauli-Blocking effects due to the occupation changes are ignored when solving BSE[13].

The self-consistent cycle starts from solving the BSE with the quasi-particle approximation. The T-matrix self-energy is then computed from electron-hole propagators with a small imaginary part of 1 meV. From the T-matrix and COHSEX self-energy, we compute the retarded spectral function and update the chemical potential. To simplify the BSE calculation in the following iterations, quasiparticle energies are extracted from the spectral functions. The self-consistent cycle is stopped when the change in chemical potential is less than 10 meV. We find that, at a wide range of excitation densities, the total spectral function consists of a quasi-particle peak and a satellite band for both the valence band and the conduction band.

SI References

1. Karni, O. *et al.* Structure of the moiré exciton captured by imaging its electron and hole. *Nature* **603**, 247–252 (2022).
2. Jakubczyk, T. *et al.* Impact of environment on dynamics of exciton complexes in a WS 2 monolayer. *2d Mater.* **5**, 031007 (2018).
3. Shao, F. *et al.* Substrate influence on transition metal dichalcogenide monolayer exciton absorption linewidth broadening. *Phys. Rev. Mater.* **6**, 074005 (2022).
4. Jakubczyk, T. *et al.* Coherence and density dynamics of excitons in a single-layer MoS2 reaching the homogeneous limit. *ACS Nano* **13**, 3500–3511 (2019).
5. Moody, G. *et al.* Intrinsic homogeneous linewidth and broadening mechanisms of excitons in monolayer transition metal dichalcogenides. *Nat. Commun.* **6**, 8315 (2015).
6. Selig, M. *et al.* Excitonic linewidth and coherence lifetime in monolayer transition metal dichalcogenides. *Nat. Commun.* **7**, 13279 (2016).
7. Mahmood, F. *et al.* Selective scattering between Floquet–Bloch and Volkov states in a topological insulator. *Nat. Phys.* **12**, 306–310 (2016).
8. Aeschlimann, S. *et al.* Survival of Floquet-Bloch states in the presence of scattering. *Nano Lett.* **21**, 5028–5035 (2021).
9. Perfetto, E., Sangalli, D., Marini, A. & Stefanucci, G. Pump driven normal-to-excitonic insulator transition: Josephson oscillations and signatures of BEC-BCS crossover in time-resolved ARPES. *Phys. Rev. Mater.* **3**, 124601 (2019).
10. Perfetto, E., Bianchi, S. & Stefanucci, G. Time-resolved ARPES spectra of nonequilibrium excitonic insulators: Revealing macroscopic coherence with ultrashort pulses. *Phys. Rev. B.* **101**, 041201 (2020).

11. Kwong, N. H., Rupper, G. & Binder, R. Self-consistent T-matrix theory of semiconductor light-absorption and luminescence. *Phys. Rev. B Condens. Matter Mater. Phys.* **79**, 155205 (2009).
12. Perfetto, E., Sangalli, D., Marini, A. & Stefanucci, G. First-principles approach to excitons in time-resolved and angle-resolved photoemission spectra. *Phys. Rev. B Condens. Matter* **94**, 245303 (2016).
13. Steinhoff, A. *et al.* Exciton fission in monolayer transition metal dichalcogenide semiconductors. *Nat. Commun.* **8**, 1166 (2017).
14. Stefanucci, G. & van Leeuwen, R. *Nonequilibrium Many-Body Theory of Quantum Systems: A Modern Introduction*. (Cambridge University Press, Cambridge, England, 2025).
15. Stolz, H. & Zimmermann, R. Correlated pairs and a mass action law in two-component Fermi systems excitons in an electron-hole plasma. *Phys. Status Solidi B Basic Res.* **94**, 135–146 (1979).
16. Perfetti, L. *et al.* Ultrafast electron relaxation in superconducting Bi(2)Sr(2)CaCu(2)O(8+delta) by time-resolved photoelectron spectroscopy. *Phys. Rev. Lett.* **99**, 197001 (2007).
17. Tao, J., Prasankumar, R. P., Chia, E. E. M., Taylor, A. J. & Zhu, J.-X. Theory of ultrafast quasiparticle dynamics in high-temperature superconductors: The dependence on pump fluence. *Phys. Rev. B Condens. Matter* **85**, 144302 (2012).
18. Wang, Y. & Zhang, F.-C. Momentum-resolved electronic relaxation dynamics ind-wave superconductors. *Phys. Rev. B Condens. Matter Mater. Phys.* **89**, 094519 (2014).

19. Sangalli, D., Dal Conte, S., Manzoni, C., Cerullo, G. & Marini, A. Nonequilibrium optical properties in semiconductors from first principles: A combined theoretical and experimental study of bulk silicon. *Phys. Rev. B Condens. Matter* **93**, 195205 (2016).
20. Pogna, E. A. A. *et al.* Photo-induced bandgap renormalization governs the ultrafast response of single-layer MoS2. *ACS Nano* **10**, 1182–1188 (2016).
21. Molina-Sánchez, A., Sangalli, D., Wirtz, L. & Marini, A. Ab initio calculations of ultrashort carrier dynamics in two-dimensional materials: Valley depolarization in single-layer WSe2. *Nano Lett.* **17**, 4549–4555 (2017).
22. Asano, K. & Yoshioka, T. Exciton–Mott Physics in Two-Dimensional Electron–Hole Systems: Phase Diagram and Single-Particle Spectra. *J. Phys. Soc. Jpn.* **83**, 084702 (2014).
23. Rohlfing, M. & Louie, S. G. Electron-hole excitations and optical spectra from first principles. *Phys. Rev. B Condens. Matter* **62**, 4927–4944 (2000).
24. Giuliani, G. & Vignale, G. *Quantum Theory of the Electron Liquid*. (Cambridge University Press, Cambridge, England, 2008).